High corrosion and wear resistant electroless Ni–P gradient coatings on aviation aluminum alloy parts

Bo Wang, Jiawei Li, Zhihui Xie, Gengjie Wang, and Gang Yu

Articles you may be interested in

Chun-duo Dai, Yu Fu, Jia-xiang Guo, and Cui-wei Du, Effects of substrate temperature and deposition time on the morphology and corrosion resistance of FeCoCrNiMo$_{0.3}$ high-entropy alloy coating fabricated by magnetron sputtering, *Int. J. Miner. Metall. Mater.*, 27(2020), No. 10, pp. 1388-1397. https://doi.org/10.1007/s12613-020-2149-2

Franco Mayanglambam and Mark Russell, Reusing oxide-based pulverised fly ash and medical waste particles to develop electroless nickel composite coatings (Ni–P/fly ash and Ni–P/SiO$_2$–Al$_2$O$_3$), *Int. J. Miner. Metall. Mater.*, 27(2020), No. 8, pp. 1147-1156. https://doi.org/10.1007/s12613-020-2071-7

L. Romero-Reséndiz, A. Flores-Rivera, I.A. Figueroa, C. Braham, C. Reyes-Ruiz, I. Alfonso, and G. González, Effect of the initial ECAP passes on crystal texture and residual stresses of 5083 aluminum alloy, *Int. J. Miner. Metall. Mater.*, 27(2020), No. 6, pp. 801-808. https://doi.org/10.1007/s12613-020-2017-0

Yong-fei Wang, Yi Guo, Sheng-dun Zhao, and Xiao-guang Fan, Direct preparation of semi-solid billets by the semi-solid isothermal heat treatment for commercial cold-rolled ZL104 aluminum alloy, *Int. J. Miner. Metall. Mater.*, 28(2021), No. 7, pp. 1164-1173. https://doi.org/10.1007/s12613-020-2067-3

Gao-hui Li, Li Zhou, Ling-yun Luo, Xi-ming Wu, and Ning Guo, Material flow behavior and microstructural evolution during refill friction stir spot welding of alclad 2A12-T4 aluminum alloy, *Int. J. Miner. Metall. Mater.*, 28(2021), No. 1, pp. 131-141. https://doi.org/10.1007/s12613-020-1998-z

Xiao-guang Sun, Peng Lin, Cheng Man, Jian Cui, Hai-bo Wang, Chao-fang Dong, and Xiao-gang Li, Prediction model for atmospheric corrosion of 7005-T4 aluminum alloy in industrial and marine environments, *Int. J. Miner. Metall. Mater.*, 25(2018), No. 11, pp. 1313-1319. https://doi.org/10.1007/s12613-018-1684-6

IJMMM WeChat   QQ author group

High corrosion and wear resistant electroless Ni–P gradient coatings on aviation aluminum alloy parts

Bo Wang[1], *Jiawei Li*[1], *Zhihui Xie*[2],✉, *Gengjie Wang*[3], *and Gang Yu*[1],✉

1) College of Chemistry and Chemical Engineering, Hunan University, Changsha 410012, China
2) Chemical Synthesis and Pollution Control Key Laboratory of Sichuan Province/College of Chemistry and Chemical Engineering, China West Normal University, Nanchong 637002, China
3) Zhongchuan Machinery Ltd. Co., Aero Engine Corporation of China, Changsha 410200, China

Abstract: A Ni–P alloy gradient coating consisting of multiple electroless Ni–P layers with various phosphorus contents was prepared on the aviation aluminum alloy. Several characterization and electrochemical techniques were used to characterize the different Ni–P coatings' morphologies, phase structures, elemental compositions, and corrosion protection. The gradient coating showed good adhesion and high corrosion and wear resistance, enabling the application of aluminum alloy in harsh environments. The results showed that the double zinc immersion was vital in obtaining excellent adhesion (81.2 N). The optimal coating was not peeled and shredded even after bending tests with angles higher than 90° and was not corroded visually after 500 h of neutral salt spray test at 35°C. The high corrosion resistance was attributed to the misaligning of these micro defects in the three different nickel alloy layers and the amorphous structure of the high P content in the outer layer. These findings guide the exploration of functional gradient coatings that meet the high application requirement of aluminum alloy parts in complicated and harsh aviation environments.

Keywords: aluminum alloy; electroless; nickel coating; corrosion; adhesion

1. Introduction

Using aluminum alloy to replace stainless steel parts is conducive to the weight reduction of the automotive and aerospace industries [1]. Moreover, high-strength aluminum and aluminum alloys can maintain good ductility even at a temperature below zero, making them appropriate for fabricating aviation devices because commercial aircraft usually works below −50°C [2–5]. 2A11 aluminum alloy classifies as the Al–Cu–Mn series and is used as the medium-strength structural parts in aircraft, such as propeller blades, bolts, and rivets [6–8]. However, the hardness of the 2A11 aluminum alloy is about HV 150, resulting in poor wear resistance. In addition, the limited corrosion resistance also restricts the broad application of aluminum alloy.

Several surface treatment methods, including electroplating, electroless plating, anodic oxidation, sol–gel, and high-energy beam surface modification, are used to improve the surface hardness and corrosion- and wear-resistance of the aluminum alloys [9]. Electroless nickel plating is commonly used among these surface modifications owing to the good corrosion and wear resistance [10–12], demonstrated on other substrates, such as magnesium alloy studied by our group [13–15]. Typical pretreatment steps for electroless nickel–phosphorus plating on aluminum alloys include zinc immer-

sion and pre-plating nickel and copper layers [8,16–17]. Zinc immersion is essential for obtaining subsequent nickel coating with desirable adhesion. The zinc immersion step is as follows: soaking the aluminum alloy into a zinc solution to form a thin layer of zinc and its compound to reduce the potential difference between the substrate and nickel coating [18]. The zinc layer can prevent the aluminum alloy surface from oxidizing again before plating. More importantly, the metallic aluminum in the aluminum alloy can be replaced by the free zinc in the solution to form a zinc layer that firmly adheres to the substrate by metal bonds and improves the adhesion of the subsequent nickel coating [19]. A two-step zinc immersion pretreatment for electroless nickel plating on aluminum alloys is recommended for achieving optimum adhesion. After the first zinc immersion, a rough zinc layer is typically produced on the aluminum alloy surface. Still, these tiny zinc crystals with poor adhesion can be dissolved and detached, and the size of these large zinc crystals can be reduced with the back-to-back dezincification in the nitric acid solution. The complete dissolution of tiny zinc crystals results in the exposure of some aluminum alloy substrate to be further reacted with the zinc solution during the second zinc immersion step. Thus, a compact zinc layer can be formed to cover most areas of the aluminum alloy surface, and the adhesion of the nickel coating can be significantly improved

---

✉ Corresponding authors: Zhihui Xie   E-mail: zhxie@cwnu.edu.cn;   Gang Yu   E-mail: yuganghnu@163.com

Ⓢ Springer

[20–21].

Based on the P content, there are three kinds of Ni–P coatings, i.e., low phosphorus (1wt%–7wt%), medium phosphorus (7wt%–10wt%), and high phosphorus (more than 10wt%). The low-phosphorus coating has high mechanical strength with a composite structure of amorphous and microcrystalline. The high-phosphorus coating has high corrosion resistance due to the amorphous structure. The Ni–P alloy gradient coating with gradient phosphorus content has been prepared to fully use the advantages of different Ni–P layers [22–24]. Georgiza *et al.* [25] compared three different types of Ni–P coatings on AZ31 magnesium alloy. They found that, compared to the single mid-phosphorus Ni–P layer, the Ni–P alloy gradient coating having a duplex structure with a mid-phosphorus inner layer and a high-phosphorus outer layer showed better corrosion resistance owing to the exclusion of diffusion paths among grain boundaries. Similarly, Hadipour *et al.* [26] found that the multilayer coating with a structure of high-phosphorus/mid-phosphorus/low-phosphorus from the copper substrate to the top surface led to a crack-free compact nodular morphology and exhibited improved wear and corrosion resistance. Therefore, it is an effective way to enhance the protective capability of the Ni–P coating by forming a gradient change of phosphorus content.

In the present work, a gradient electroless Ni–P coating with a triple-layered structure of low-phosphorus/mid-phosphorus/high-phosphorus from the substrate to the surface was prepared on the 2A11 aluminum alloy. The effects of the temperature and time of the two-step zinc immersion procedure on the coating performance were investigated to achieve a coating with both strong adhesion and high corrosion/wear resistance to meet the high requirement of aluminum alloy parts applied in harsh environments. The interface morphology and element distribution of the coating were also characterized through scanning electron microscope (SEM), energy dispersive spectroscopy (EDS), and X-ray diffraction (XRD) techniques.

2. Experimental

2.1. Materials

2A11 aluminum alloy was used as substrate and was cut

into a dimension of 30 mm × 50 mm × 5 mm. The composition of the aluminum alloy is shown in Table 1.

Table 1.   Chemical composition of aviation 2A11 aluminum alloy   wt%

Si	Fe	Cu	Mg	Other	Al
<0.7	0.7	3.8–4.8	0.4–0.8	0.6	Balance

2.2. Method

The aluminum alloy was first polished with water sandpaper (from 800# to 2000#) and then cleaned for later use. The pretreatment flow of aluminum alloy and electroless nickel plating procedure is shown in Fig. 1. Zinc immersion removes the natural aluminum oxide film on the aluminum alloy surface by depositing a thin replacement layer with good bonding strength in the zincate solution. This layer can not only prevent the natural aluminum oxide from regeneration but is also helpful for the following deposition of other metal coatings. After the degreasing and first zinc immersion steps, the time for the second zinc immersion is 60 s during the investigation of the effects of zinc immersion temperature (10, 15, 25, and 35°C); the temperature for the second zinc immersion is 25°C during the investigation of the effects of zinc immersion time (10, 30, 60, and 90 s). The Ni–P alloy gradient coating was obtained by sequential immersing the substrate into the alkaline low-phosphorus, acidic medium-phosphorus, and acidic high-phosphorus plating baths. The bath compositions and operating conditions are shown in Table 2. After each step, the samples were washed twice with deionized water to avoid contamination from the previous step.

2.3. Coating performance test

2.3.1. Coating surface morphology, chemical composition and phase structure

A scanning electron microscope (SEM, JSM-7900F) was used to observe the surface morphology of the sample with the zinc immersion layer and Ni–P coating and measure the thickness of each coating. The attached energy dispersive spectrometer (EDS, JSM-7900F) was used to determine the composition of the coating. An X-ray diffractometer (XRD-7000) was used to analyze the phase structure of the layer.
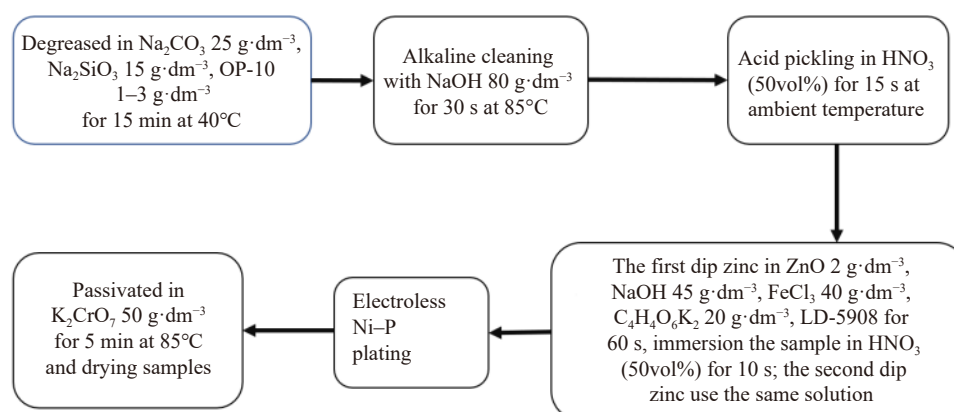

Fig. 1.   Flow chart for preparation of electroless Ni–P coating on 2A11 aluminum alloy.

Table 2. **Composition and operating conditions of plating solutions for deposition of three electroless Ni–P layers with different P contents**

Sample	Compositions	Operating conditions
Low P	$NiSO_4 \cdot 6H_2O$ 30 g·dm^{-3}, $NaH_2PO_2 \cdot H_2O$ 25 g·dm^{-3}, $C_6H_5Na_3O_7 \cdot 2H_2O$ 30 g·dm^{-3}, NH_4Cl 10 g·dm^{-3}, LD-5420 (additive)	40°C, 8–15 min, pH 9.0, stirring 10 r/min
Medium P	$NiSO_4 \cdot 6H_2O$ 15 g·dm^{-3}, CH_3COONa 13 g·dm^{-3}, NH_4HF_2 8.5 g·dm^{-3}, HF (50wt%) 10 cm^3·dm^{-3}, $NaH_2PO_2 \cdot H_2O$ 14 g·dm^{-3}, thiourea 1 mg·dm^{-3}, ammonia, LD-5904 (additive)	90°C, 90 min, pH 4.8, air stirring
High P	$NiSO_4 \cdot 6H_2O$ 21 g·dm^{-3}, $C_3H_6O_2$ 3 cm^3·dm^{-3}, $C_3H_6O_3$ 23 cm^3·dm^{-3}, $NaH_2PO_2 \cdot H_2O$ 24 g·dm^{-3}, thiourea 1 mg·dm^{-3}, ammonia, LD-5905 (additive)	90°C, 120 min, pH 4.8, air stirring

2.3.2. Corrosion resistance

The polarization curves and electrochemical impedance spectroscopy (EIS) were obtained by an electrochemical station (Gamry, Interface 1000) and were used to evaluate the corrosion resistance of the coating [27]. The measurement was carried out in a 3.5wt% NaCl solution with a three-electrode cell system composed of a saturated calomel electrode as the reference, a platinum sheet as auxiliary electrodes, and the samples with an effective area of 1.0 cm^2 as the working electrodes. The samples were firstly immersed in a 3.5wt% aqueous NaCl solution for one hour at least until the open circuit potential stabilized before the electrochemical tests performed.

2.3.3. Adhesion

(1) Scratch method.

According to JB/T 8554-1997 standard, a multifunctional material surface performance testing machine (MFT-4000) was used to determine the adhesion of the coating. The coating was cut deeply in a lattice pattern, and the bonding force of the layer was evaluated by measuring the critical load of the adhesion failure of the coating–matrix interface.

(2) Bending method.

The bending test was carried out according to the GB/T 5270-200x method. The specimen was repeatedly bent to 180° along an axis with a diameter equal to the thickness of the specimen. After the bending, the adhesion was evaluated by observing whether the section was peeled.

2.3.4. Microhardness

A digital Vickers Indenter was used to measure the microhardness of the coating with a load of 0.49 N for lasting 5 s. The average value for each sample was calculated based on the hardness at five points.

2.3.5. Wear and friction performance

The Taber enhanced abrasion tester (SR-5612B) was used for the wear test. The test conditions included a grinding wheel with a particle size of 0.01 mm, an applied load of 9.8 N, a rotation speed of 60 r/min, and a wear time of 300 s. The wear resistance of different coatings was evaluated by calculating the wear rate (v) via the following formula:

$$v = \frac{W_0 - W_1}{\rho S t} \tag{1}$$

where v is the wear rate, cm·min^{-1}; W_0 and W_1 are the mass before and after abrasion, g; ρ is the density of the coating material, g·cm^{-3}, which is 2.8 g·cm^{-3} for aluminum alloy, and 7.9 g·cm^{-3} for nickel–phosphorus alloy; t is the wear time, min; S is the area of the wear surface, cm^2.

3. Results and discussion

3.1. Influence of the zinc immersion process on coating performance

Fig. 2 shows the morphologies of the zinc layer prepared at different temperatures. It can be observed that the zinc grains gradually dissolved as the temperature increased. The large zinc grains became smaller to produce a uniform zinc layer with increasing temperature. The zinc layer obtained at a low temperature was thin and porous, and cannot meet the requirements of an intermediate layer. These spherical zinc grains preferentially grew at highly active sites along the edges of the pores (10°C). When the temperature increased to 15°C, the zinc layer showed a denser morphology with smaller pore diameters and more uniform zinc grains. When the zinc immersion temperature rose to 25°C, the zinc layer showed a surface morphology with much lesser and shallower cavities, which harms the mechanical bonding between the substrate and coating. Further, with the temperature increased to 35°C, holes cannot be obtained, forming a Ni–P layer with poor adhesion. Noting that although the dense morphology with small pore diameters and uniform zinc grains of the zinc layer formed at 15°C helps give rise to good mechanical bonding between the substrate and coating, it also provides a large number of active areas resulting in a high initial deposition rate and porous layer in the initial deposition period which harms to the adhesion. Therefore, the temperature of 25°C was chosen for further optimizing the secondary zinc immersion time.

Fig. 3 shows the morphologies of the zinc layers after a secondary zinc immersion at different times on the surface of the first zinc layer. When the zinc immersion time was short (10 s), the zinc layer was not uniformly covered by the newly formed zinc layer. Many obvious holes acting as corrosion pathways to corrode the substrate during plating could also be observed. When the zinc immersion time was increased to 30 s, the porosity of the zinc layer decreased significantly, which could reduce the corrosion pathways by the plating bath. It is worth noting that these pores are also helpful in providing a good interlocking between the substrate and coating to improve adhesion. Further prolonging the time to 60 and 90 s, very dense and even new zinc layers with many zinc grains were formed. Such layers are hard to produce strong adhesion for the subsequent Ni–P layer, which would be confirmed later by the adhesion test result.
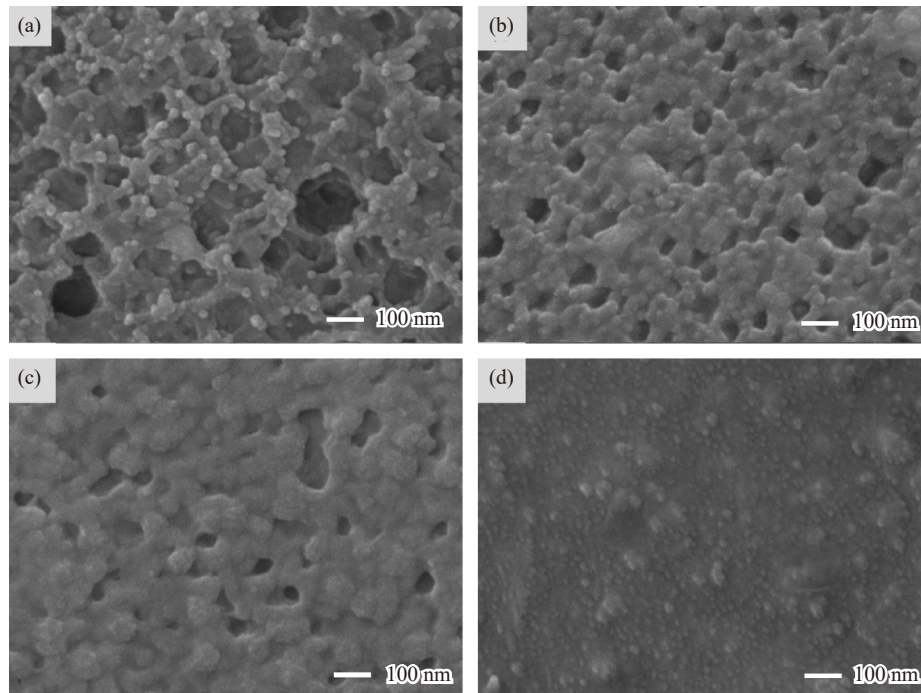
Fig. 2.   Surface morphologies of the zinc layer obtained at different immersion temperatures: (a) 10, (b) 15, (c) 25, and (d) 35°C for 30 s.
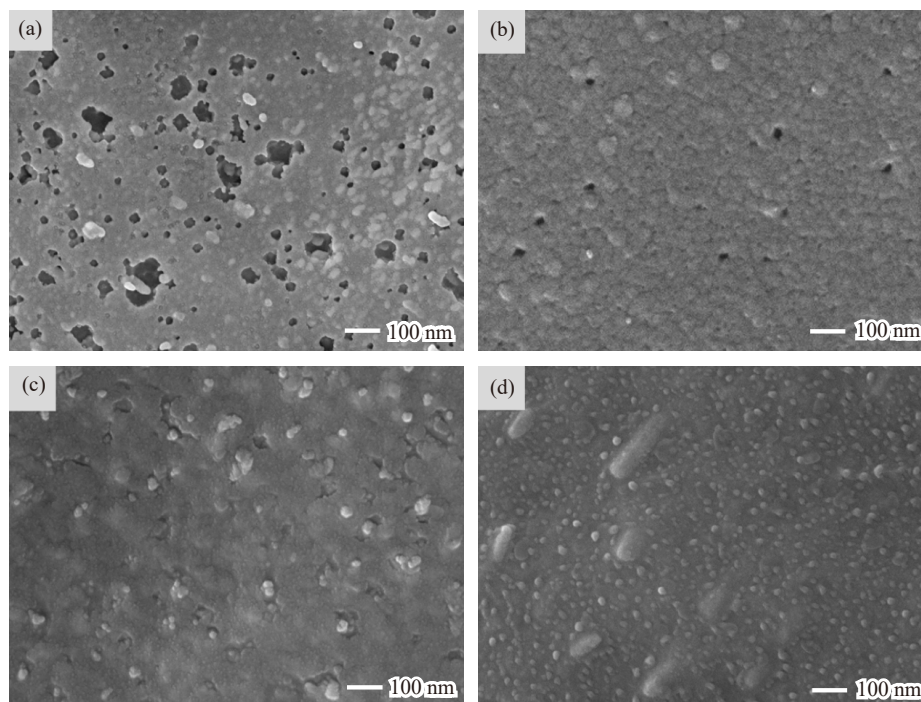

Fig. 3.   Surface morphologies of the zinc layer after a secondary zinc immersion treatment with different times: (a) 10, (b) 30, (c) 60, and (d) 90 s at 25°C.

3.2. Surface morphology, composition and structure of the different Ni–P coatings

The surface morphologies of the three Ni–P coatings with different P contents are shown in Fig. 4(a)–(c). Fig. 4(a) shows the surface morphology of the Ni–P coating with a low-P content. Many concavities and small particles can be observed clearly on the coating surface, suggesting that some of the cavities formed during pretreatment were not filled completely by the Ni–P alloy, and many Ni–P crystal nuclei were not well integrated into an intact nickel coating. This unregular morphology is ascribed to the thin thickness of the low-P content Ni–P film, which will be confirmed later by the cross-sectional SEM image. In the cases of low-P/medium-P double-layer and low-P/medium-P/high-P triple-layer coatings, typical "cauliflower" morphologies with many nodules were formed, demonstrating the formation of Ni–P alloy coatings. Although the double-layered nickel coating surface was slightly rougher than that of the triple-layered coating
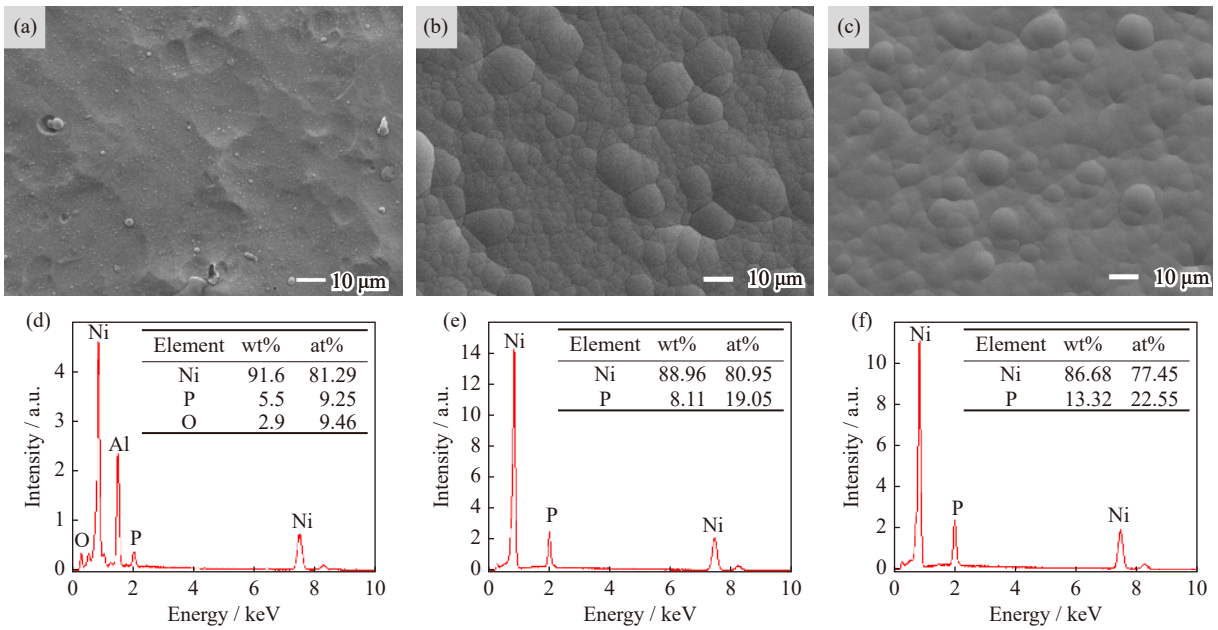
Fig. 4.   SEM images (a–c) and EDS spectra (d–f) of the three coatings with different P contents: (a, d) low P; (b, e): medium P; (c, f): high P.

because of the more significant variation in diameter of these nodules, both are compact without evident pinholes or defects and are expected to show good corrosion resistance. According to the EDS spectra, as shown in Fig. 4(d)–(f), the apparent content of O element (2.9wt%) was identified in the low-P Ni–P coating. The O element results from the oxide film formed during the pretreatment process. The aluminum element comes from the aluminum alloy matrix, demonstrating the low-P Ni–P film' thin thickness and limited corrosion resistance. For comparison, the Al element with high content in the low-P Ni–P film was excluded while calculating the element ratio in the different Ni–P layers because it comes from the substrate rather than the coating. The O element cannot be identified. The P content increased to 8.11wt% for the double-layered coating and 13.32wt% for the triple-layered coating, manifesting amorphous structural Ni–P layers with good corrosion resistance were probably deposited.

The X-ray diffractometer identified the phase structures of the three different coatings. The corresponding results are shown in Fig. 5. The XRD pattern shows prominent and sharp diffraction peaks at 2θ = 38°, 45°, 65°, and 78° for the

low P layer, indicating that the coating was mainly composed of crystalline phases. Based on the PDF file (JCPDS card No.: Ni 03-1051, 88-2326; $N_{12}P_5$ 74-1381; Ni_3P 65-2778), these peaks matched well with the microcrystalline Ni and amorphous $Ni_{12}P_5$ and amorphous Ni_3P alloy. For the middle-P and high-P coatings, only a broad diffraction peak with a 2θ angle of around 45° was observed in the XRD patterns, which is attributed to the diffraction of the nickel (111) plane. Furthermore, the peak in the XRD pattern for high-P coating is wider than that for the middle-P coating owing to the relatively high P content and more content of amorphous phase structure in the former sample [28]. The high content of P element in the Ni crystal lattice results in forming a Ni-based supersaturated solid solution and amorphous structure, which is usually expected to improve the corrosion and wear resistance of the coatings. This is because an amorphous coating structure does not have the crystal characteristics of a crystalline alloy, such as the easy occurrence of micro-galvanic corrosion.

Fig. 5(b) shows the cross-sectional morphology of the combined gradient Ni–P coating. The thickness and com-
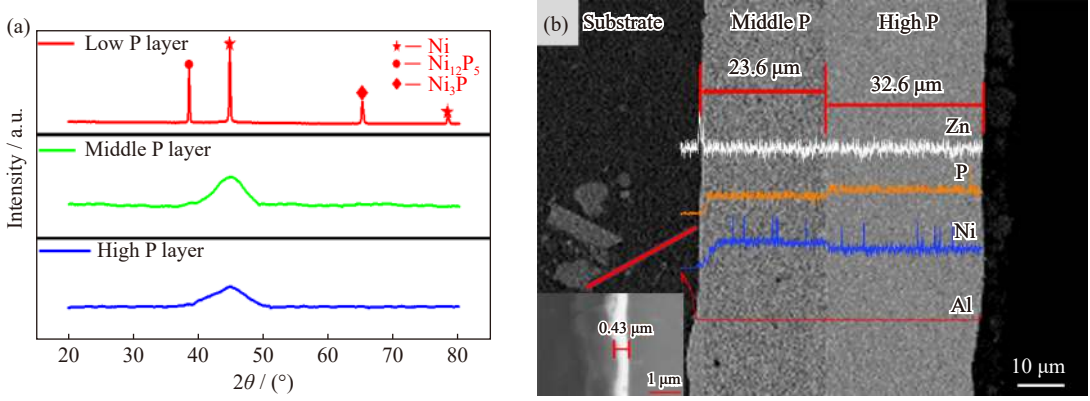

Fig. 5.   (a) XRD patterns of the Ni–P layers with different P contents; (b) cross-sectional morphology of the gradient Ni–P coating.

pactness of a cathodic layer are key factors affecting the protective effect of the Al substrate. The coating porosity decreases with increasing thickness. When the thickness reaches a specific value, the coating becomes denser, and the porosity is evenly reduced to zero. It can be seen from Fig. 5 that the middle-P and high-P coatings are very smooth, showing thicknesses of 23.6 μm for the middle P layer and 32.6 μm for the high P layer. At the same time, the line-scan EDS test can see the variations of different elements across the gradient coating. The double compact coatings can effectively protect the Al substrate from corrosion. Fig. 5(b) also shows that the low-P layer has a thickness of only 0.43 μm (inset in Fig. 5(b)). Because it is too thin, the transition layer must be observed in magnification. It was found that crests and grooves were not observed at the interface between the substrate and the coating, indicating the strong adhesion of the coating. The zinc layer, named the "soft transition" zone, can increase the adsorption capacity between the Ni–P plating and Al substrate to improve the bonding force. Besides, the middle-P coating between the low-P and high-P coatings is conducive to reducing the strains and improving the bonding strength of the gradient coating due to preventing mutations of phosphorus content between layers.

3.3. Corrosion resistance of the different Ni–P coatings

Defects among the nodules and micropores in the electroless nickel layer can quickly become a diffusion channel for the corrosive media, decreasing the corrosion protection of the coating and causing substrate destruction. Reducing the defects and especially through-pores in the nickel layer are effective ways to improve the corrosion protection for aluminum alloy. However, it is difficult to eliminate the micropores in a single electroless nickel layer owing to the hydrogen evolution during plating. Gradient coating with a combination of different nickel layer phases is expected to reduce the through pores and enhance the protection for aluminum alloy because electroless nickel layers with different phosphorus contents have different microstructures and pore defects. According to the results of the polarization curves, as

shown in Fig. 6(a), it can be seen that the gradient plating obtained by combining three nickel layers with different phosphorus contents has a significant positive shift in the self-corrosion potential and the lowest corrosion current density, indicating a substantial improvement in the corrosion resistance. The considerable increase in the corrosion protection of the gradient plating is attributed to the amorphous structure of the nickel layer with high phosphorus content on the surface and the triple-layered nickel coating with different defects that could increase the difficulty of forming through-holes. The amorphous structure of the high nickel layer makes the nickel layer itself less susceptible to the formation of micro galvanic corrosion. It has significantly better corrosion resistance than the crystalline nickel–phosphorus alloy layer. Meanwhile, it has been demonstrated that the surface of the amorphous nickel–phosphorus alloy layer is easy to form an oxide film with high corrosion resistance. In addition, according to the SEM images, the low-P/medium-P/high-P gradient coating shows the most uniform and dense surface morphology, which is undoubtedly one of the reasons for the best corrosion resistance.

Electroless impedance spectroscopy (EIS) was used to compare the corrosion resistance of the coatings, which were soaked in a 3.5wt% NaCl solution. Fig. 7 shows the Nyquist and Bode plots of each coating. The EIS spectrum was analyzed using an equivalent circuit model shown in Fig. 7(a) (inset). In this model, R_s, R_c, and R_{ct} represent the resistance of the solution, the coatings, and the charge transfer resistance, respectively. C_1 and C_2 are the capacitance of the coating and the electric double layer. A constant phase element (CPE) replaces pure capacitance [29–31]. The impedance of CPE can be described as follows:

$$Z_{CPE} = \frac{1}{Y_0(\omega j)^n},$$

where ω is the angular frequency, j is the imaginary number, Y_0 is the admittance function, and n is the coefficient related to the deviation. As shown in Fig. 7, the Nyquist diagrams of different combinations of nickel layers show similar shapes in the relatively same frequency region, indicating that the
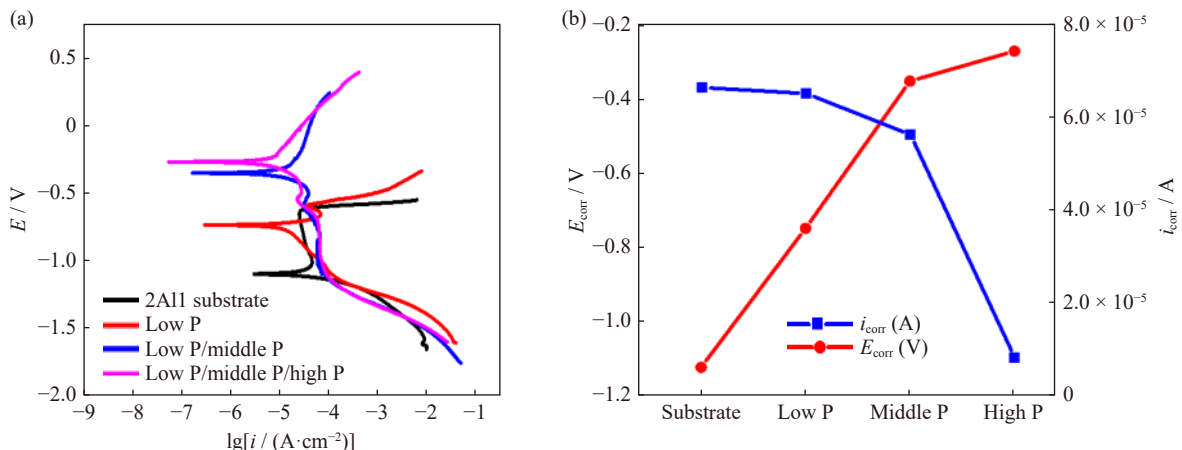

Fig. 6. **(a) Polarization curves of different Ni–P layers on the aluminum alloy in a 3.5wt% NaCl solution and (b) the corresponding Tafel parameters. *E* and *i* are the polarization potential and corresponding current density, respectively; *i*corr and *E*corr are the corrosion current density and corrosion potential, respectively.**
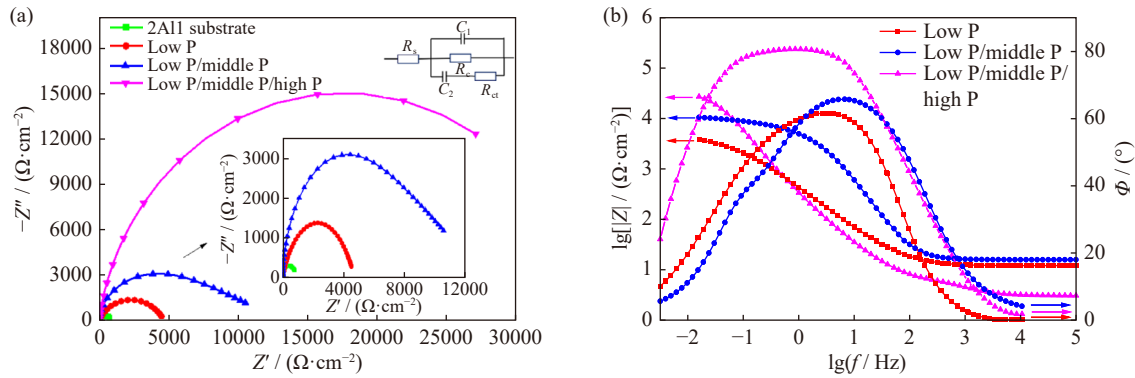
Fig. 7. EIS plots of various electroless Ni–P layers in a 3.5% NaCl solution: (a) Nyquist plots; (b) Bode plots. The abscissa and ordinate in (a) are the real part and imaginary part of the impedance, respectively; the abscissa in (b) is the logarithm of frequency, and the ordinates at the left and right hands in (b) are the logarithm of impedance modulus and phase angle of impedance, respectively.

electrochemical processes occurring at the coating surface are roughly the same. However, Table 3 shows that the R_{ct} value of the low-P/middle P/high-P gradient coatings is much higher than those of single low-phosphorus nickel layer and duplex low-P/middle P gradient coatings, showing higher corrosion resistance in the studied corrosive media [32].

The salt spray test was carried out in a neutral 5wt% sodium chloride salt at 35°C. The coatings with different P contents were placed in the salt spray box. The visual photos and corresponding SEM images of the different Ni–P coatings after salt spray corrosion are shown in Fig. 8. After 96 h of salt spray test, many corrosion spots appeared at the surface of the single nickel layer with low-phosphorus (Fig. 8(a)). The coating surface has noticeable color changes with some blackened and cracked areas. The corresponding SEM images further prove that the surface was corroded seriously

(Fig. 8(d)). These areas with obvious corrosion holes probably lost the corrosion protection function, indicating that the corrosion resistance of the single nickel layer with a low phosphorus content is poor, and it is challenging to protect the aluminum alloy from corrosion. When the salt spray test time was increased to 336 h, the low P/medium-P duplex coating did not show corrosion holes, peeling, blistering, flaking, or other phenomena on the macroscopic level. Still, there were color changes and a few corrosion spots on the edge of the specimen. Moreover, corrosion phenomena with an accumulation of corrosion products in some areas and even a tiny amount of microcracks can be observed at the surface of the coating from the SEM image (Fig. 8(e)). It can be speculated that these small corrosion areas will expand and become more profound, resulting in failed protection with increasing salt spray time. In contrast, discoloration and

Table 3. Fitted EIS electrochemical parameters for different electroless Ni–P layers

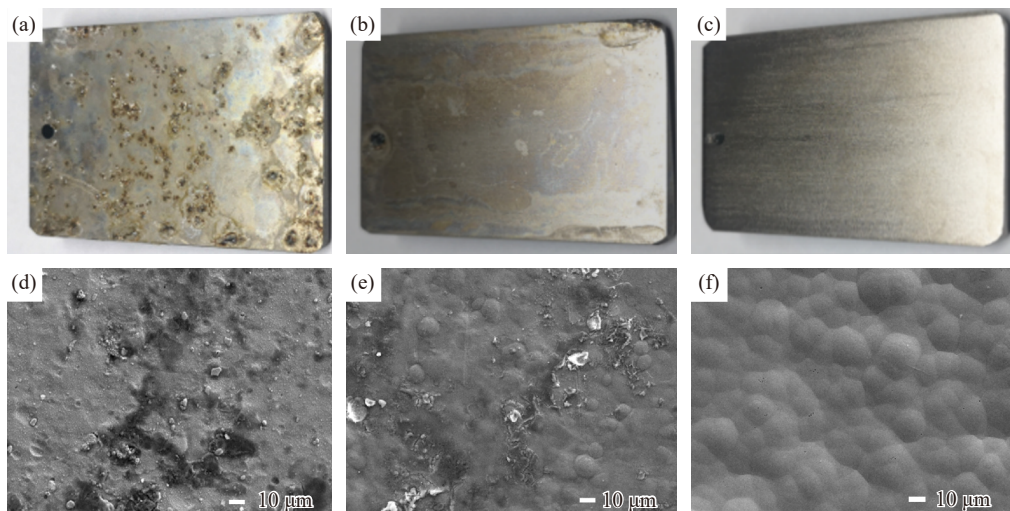| Samples	R_s / $(\Omega \cdot cm^2)$	R_{ct} / $(\Omega \cdot cm^2)$	R_c / $(\Omega \cdot cm^2)$	C_1 / $(S \cdot s^n \cdot cm^{-2})$	C_2 / $(S \cdot s^n \cdot cm^{-2})$
Al substrate	8.049	657	0.2864	4.124×10^{-14}	6.549×10^{-5}
Low P	3.289	4867	135.5	4.748×10^{-5}	1.230×10^{-4}
Low-P/medium-P	3.170	10531	231.3	6.430×10^{-5}	3.807×10^{-4}
Low-P/medium-P/high-P	3.305	28075	851.6	3.931×10^{-5}	4.529×10^{-4}

Fig. 8. (a–c) Digital pictures and (d–f) SEM images of the different Ni–P layers after the salt spray test with different hours: (a, d) low-P coating, 96 h; (b, e): low-P/medium-P, 336 h; (c, f) low-P/medium-P/high-P, 500 h.

noticeable corrosion pits are not visually observed on the surface of the low-P/medium-P/high-P triple-layered gradient coating, even after the salt spray time increased to 500 h. The surface of the layer remains bright and flat, and corrosion signs are not found even at the edges of the hole for hanging the sample. Microscopically, the gradient coating is still flat and smooth without any signs of corrosion among the different nodules (Fig. 8(f)). The evident micromorphological difference of the triple-layered coating compared with that before the salt spray test is not observed, indicating that the as-designed gradient coating can continuously protect the aluminum alloy substrate from corrosion under a long-time salt spray attack environment. In conclusion, the results of the above electrochemical tests show that the corrosion resistance of the low-P/medium-P/high-P gradient coating is significantly better than those of the single nickel layer low phosphorus coating and the duplex low-P/medium-P coating and can fully meet the practical requirements of aluminum alloy products in the aerospace industry.

3.4. Bonding force, microhardness and wear resistance

Two methods, including an automatic scratch test and a bending test, were used to evaluate the adhesion of the Ni–P coatings with different P contents prepared by different pretreatments. As shown in Fig. 9, the Ni–P coating prepared with a zinc immersion time of 30 s and temperature of 25°C exhibits a relatively better bonding force. The coating obtained at the optimum condition shows a highest critical load exceeding 80 N. Unsuitable temperature (too low or too high)

or time (too short or too long) will adversely affect the bonding between the coating and substrate.

The bending test consolidated these adhesion results based on the automatic scratch test. As shown in Fig. 10, inappropriate temperature or time caused the coating to peel severely after the bending test. The Ni–P coating obtained with the optimum condition did not peel off after a bending higher than 90 degrees, manifesting excellent adhesion.

A Taber wear tester was used to measure the wear resistance of the different Ni–P coatings, shown in Fig. 11. The single Ni–P layer with a low P content is only several microns and is an intermediate layer. Thereby, the wear resistance is not discussed here. The bare aluminum alloy shows a high mass loss with a wear rate of 199.6 $\mu m \cdot h^{-1}$. After deposition of the low-P/medium-P double-layer or low-P/medium-P/high-P gradient coatings, the wear rate drops significantly to 64.5 and 70.6 $\mu m \cdot h^{-1}$, respectively. The significant decrease in wear rate suggests an evident improvement in wear resistance. Compared to the double-layer coating, the wear rate of the triple-layered coating increases slightly, which is attributed to a minor decrease in the hardness of the high P coating. It is well-known that wear resistance is related to hardness [33]. As the P content increases, the large amount of soft "γ" structure in the coating reduces the hardness and wear resistance [34].

A microhardness tester was used to obtain the microhardness of the aluminum alloy with and without Ni–P coatings (Fig. 11(b)). It can be seen from Fig. 11 that the microhardness of the Ni–P alloy gradient coating is about HV 503,
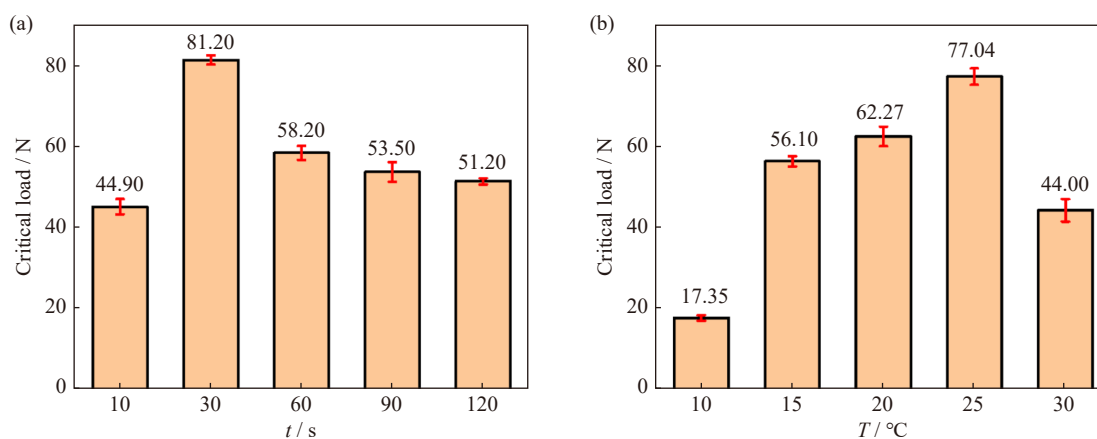

Fig. 9. Effects of the (a) secondary zinc immersion times (*t*) and (b) zinc immersion temperatures (*T*) on the critical load of the Ni–P coatings in the scratch test.
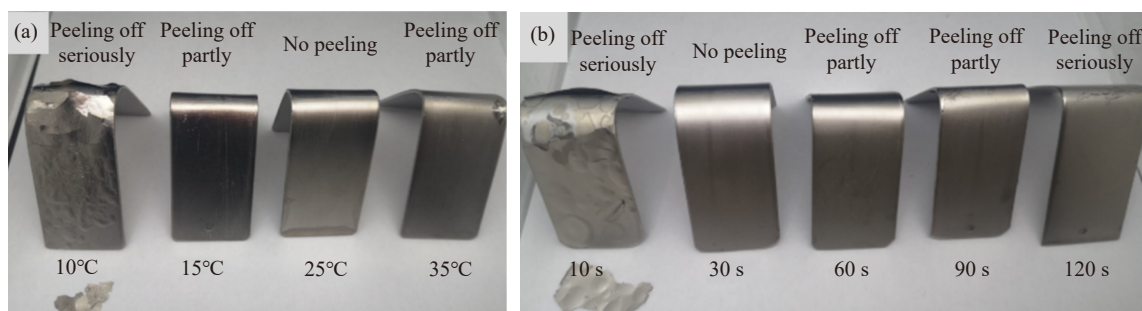

Fig. 10. Digital pictures showing the effects of (a) zinc immersion temperatures and (b) secondary zinc immersion times on the adhesion of the Ni–P layer on the aluminum alloy after the bending test method.
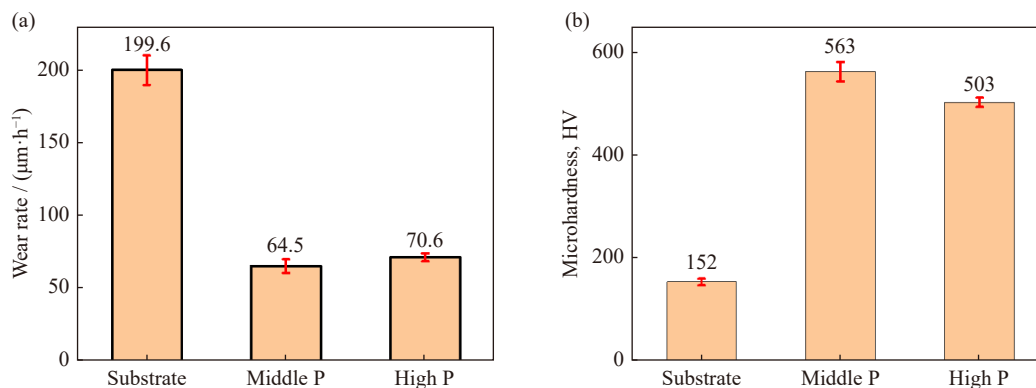
Fig. 11.   (a) Wear rate and (b) Vickers microhardness of the aluminum alloy with and without different electroless Ni–P layers.

which is about three times that of the substrate (HV 152), indicating that electroless Ni–P plating can significantly increase the microhardness of the substrate. The results show that the electroless Ni–P coating in this study has strong bonding force, high hardness, and wear resistance.

4. Conclusions

A gradient coating of low-phosphorus, medium-phosphorus, and high-phosphorus electroless Ni–P layers was deposited on the aviation aluminum alloy surface through a two-step zinc immersion pretreatment method. The low-phosphorus layer (~1 µm) has a crystalline structure with a phosphorus content of about 5wt%. The medium-phosphorus layer (23.6 µm) with a phosphorus content of about 8wt% and the high-phosphorus layer (32.6 µm) with a phosphorus content of about 13wt% are amorphous structures and dense without apparent defects. The Ni–P alloy gradient coating with multiple Ni–P layers showed good adhesion and high corrosion and wear resistance.

The zinc immersion temperature and time significantly impact the morphology and bonding force of the Ni–P alloy gradient coating. The zinc layer obtained at a low temperature below 15°C is uneven and has large pores. The grain size of the zinc layer gradually increased and became more uniform with the increased zinc immersion temperature. The zinc immersion layer formed at 25°C for 30 s showed the best uniformity, producing good adhesion and corrosion resistance for the Ni–P alloy gradient coating.

The wear resistance was directly related to the hardness of the Ni–P coating. As the phosphorus content increased, the hardness of the Ni–P coating decreased, resulting in reduced wear resistance. The wear resistance of the low-phosphorus/middle-phosphorus duplex-layer coating was better than that of the low-phosphorus/middle-phosphorus/high-phosphorus triple-layer coating. However, the triple-layered coating showed the best corrosion resistance compared with other composite coatings and is suitable as a protective coating for aluminum alloy used in harsh environments.

Acknowledgement

Conflict of Interest

Zhihui Xie is a youth editorial board member for this journal and was not involved in the editorial review or the decision to publish this article. The authors declare that there is no conflict of interest.

References

[1]   S. Basak, P. Biswas, S. Patra, H. Roy, and M.K. Mondal, Effect of TiB$_2$ and Al$_3$Ti on the microstructure, mechanical properties and fracture behaviour of near eutectic Al–12.6Si alloy, *Int. J. Miner. Metall. Mater.*, 28(2021), No. 7, p. 1174.

[2]   Y. Jafari-Tarzanagh, D. Seifzadeh, A. Khodayari, and R. Samadianfard, Active corrosion protection of AA2024 aluminum alloy by sol–gel coating containing inhibitor-loaded mesoporous SBA-15, *Prog. Org. Coat.*, 173(2022), art. No. 107166.

[3]   Y.J. Tarzanagh, D. Seifzadeh, Z. Rajabalizadeh, A. Habibi-Yangjeh, A. Khodayari, and S. Sohrabnezhad, Sol–gel/MOF nanocomposite for effective protection of 2024 aluminum alloy against corrosion, *Surf. Coat. Technol.*, 380(2019), art. No. 125038.

[4]   S. Yadav, S.P. Tewari, J.K. Singh, and S.C. Ram, Effects of mechanical vibration on the physical, metallurgical and mechanical properties of cast A308 (LM21) aluminum alloy, *Int. J. Miner. Metall. Mater.*, 29(2022), No. 6, p. 1206.

[5]   Z. Shao, L. Cui, L.J. Yang, *et al.*, Microstructure and mechanical properties of friction pull plug welding for 2219-T87 aluminum alloy with tungsten inert gas weld, *Int. J. Miner. Metall. Mater.*, 29(2022), No. 6, p. 1216.

[6]   C. Duraipandi, A. Khan M, J.J.T. Winowlin, N.M. Ghazaly, and P.M. Mashinini, Solid particle erosion studies of thermally deposited alumina–titania coatings on an aluminum alloy, *Int. J. Miner. Metall. Mater.*, 28(2021), No. 7, p. 1186.

[7]   H. Ebrahimzadeh, H. Farhangi, S.A.A.A. Mousavi, and A. Ghahramani, Microstructural analyses of aluminum–magnesium–silicon alloys welded by pulsed Nd:YAG laser welding, *Int. J. Miner. Metall. Mater.*, 27(2020), No. 5, p. 660.

[8]   A.G.G. Gutiérrez, M.A. Pech-Canul, and P.J. Sebastian, Zincating effect on corrosion resistance of electroless Ni–P coating on aluminum alloy 6061, *Fuel Cells*, 17(2017), No. 6, p. 770.

[9]   S. Nezamdoust and D. Seifzadeh, rGO@APTES/hybrid sol–gel nanocomposite for corrosion protection of 2024 aluminum alloy, *Prog. Org. Coat.*, 109(2017), p. 97.

[10] I. Fatima, O. Fayyaz, M.M. Yusuf, A. Al Ashraf, and R.A. Shakoor, Enhanced electrochemical and mechanical performance of BN reinforced Ni–P based nanocomposite coatings, *Diam. Relat. Mater.*, 130(2022), art. No. 109454.

[11] M.H. Sliem, O. Fayyaz, R.A. Shakoor, *et al.*, The influence of

different preparation methods on the erosion behavior of NiP–ZrO$_2$ nanocomposite coating, *Tribol. Int.*, 178(2023), art. No. 108014.

[12] C.O. Osifuye, A.P.I. Popoola, C.A. Loto, and D.T. Oloruntoba, Effect of bath parameters on electroless Ni–P and Zn–P deposition on 1045 steel substrate, *Int. J. Electrochem. Sci.*, 9(2014), No. 11, p. 6074.

[13] Z.H. Xie, D. Li, Z. Skeete, A. Sharma, and C.J. Zhong, Nanocontainer-enhanced self-healing for corrosion-resistant Ni coating on Mg alloy, *ACS Appl. Mater. Interfaces*, 9(2017), No. 41, p. 36247.

[14] Y.Q. Li, Y.J. Ouyang, R. Fang, *et al.*, A nickel-underlayer/LDH-midlayer/siloxane-toplayer composite coating for inhibiting galvanic corrosion between Ni layer and Mg alloy, *Chem. Eng. J.*, 430(2022), art. No. 132776.

[15] Z.W. Song, Z.H. Xie, L.F. Ding, Y.J. Zhang, and X.Y. Hu, Preparation of corrosion-resistant MgAl-LDH/Ni composite coating on Mg alloy AZ31B, *Colloids Surf. A*, 632(2022), art. No. 127699.

[16] M. Kocabaş, C. Örnek, M. Curioni, and N. Cansever, Nickel fluoride as a surface activation agent for electroless nickel coating of anodized AA1050 aluminum alloy, *Surf. Coat. Technol.*, 364(2019), p. 231.

[17] F. Delaunois, J.P. Petitjean, P. Lienard, and M. Jacob-Duliere, Autocatalytic electroless nickel–boron plating on light alloys, *Surf. Coat. Technol.*, 124(2000), No. 2-3, p. 201.

[18] X.C. Wei, J.B. Wang, X.M. Zhang, and X.G. Wang, Study on the development of pretreatment processes of electroless nickel plating on Al alloy surface, *Mater. Sci. Forum*, 809-810(2014), p. 412.

[19] S. Wernick, R. Pinner, and P.G. Sheasby, *The Surface Treatment and Finishing of Aluminum and Its Alloys*, 6th ed., ASM International Materials Park, OH, 2001.

[20] C.H. Zhang, X.M. Huang, N. Sheng, and L.L. Gao, A zinc dipping technique for Mg–16Li–5Al–0.5RE alloy at room temperature, *Mater. Corros.*, 64(2013), No. 6, p. 509.

[21] I.S. Othman, M.J. Starink, and S.C. Wang, Impact of single and double zincating treatment on adhesion of electrodeposited nickel coating on aluminium alloy 7075, *J. Adv. Manuf. Technol.*, 12(2018), p. 179.

[22] D.D.N. Singh and R. Ghosh, Electroless nickel–phosphorus coatings to protect steel reinforcement bars from chloride induced corrosion, *Surf. Coat. Technol.*, 201(2006), No. 1-2, p. 90.

[23] J.D. Lin and C.T. Chou, The influence of phosphorus content on the microstructure and specific capacitance of etched electroless Ni–P coatings, *Surf. Coat. Technol.*, 368(2019), p. 126.

[24] Y.F. Li, K. Zhang, M.M. Zhang, T.T. Wu, P. Cao, and W. Gao, Preparation of electroless Ni–P alloy coating with medium temperature and low phosphorus content, *Int. J. Mod. Phys. B*, 34(2020), art. No. 2040044.

[25] E. Georgiza, J. Novakovic, and P. Vassiliou, Characterization and corrosion resistance of duplex electroless Ni–P composite coatings on magnesium alloy, *Surf. Coat. Technol.*, 232(2013), p. 432.

[26] A. Hadipour, M. Rahsepar, and H. Hayatdavoudi, Fabrication and characterisation of functionally graded Ni–P coatings with improved wear and corrosion resistance, *Surf. Eng.*, 35(2019), No. 10, p. 883.

[27] F.L. Zheng, H.S. Chen, Y.Q. Zhang, W.X. Wang, and H.H. Nie, Microstructure evolution and corrosion resistance of AZ31 magnesium alloy tube by stagger spinning, *Int. J. Miner. Metall. Mater.*, 29(2022), No. 7, p. 1361.

[28] L.D. Ma, G. Lü, and X.L. Shen, An investigation of chemically deposited Ni–P alloys by EXAFS and XRD, *Chin. J. Chem.*, 8(1990), No. 3, p. 239.

[29] M. Rahsepar, F. Mohebbi, and H. Hayatdavoudi, Synthesis and characterization of inhibitor-loaded silica nanospheres for active corrosion protection of carbon steel substrate, *J. Alloys Compd.*, 709(2017), p. 519.

[30] H. Hayatdavoudi and M. Rahsepar, A mechanistic study of the enhanced cathodic protection performance of graphene-reinforced zinc rich nanocomposite coating for corrosion protection of carbon steel substrate, *J. Alloys Compd.*, 727(2017), p. 1148.

[31] H. Hayatdavoudi and M. Rahsepar, Smart inhibition action of layered double hydroxide nanocontainers in zinc-rich epoxy coating for active corrosion protection of carbon steel substrate, *J. Alloys Compd.*, 711(2017), p. 560.

[32] H. Luo, M. Leitch, Y. Behnamian, Y.S. Ma, H.B. Zeng, and J.L. Luo, Development of electroless Ni–P/nano-WC composite coatings and investigation on its properties, *Surf. Coat. Technol.*, 277(2015), p. 99.

[33] E.M. Fayyad, A.M. Abdullah, M.K. Hassan, A.M. Mohamed, G. Jarjoura, and Z. Farhat, Recent advances in electroless-plated Ni–P and its composites for erosion and corrosion applications: A review, *Emergent Mater.*, 1(2018), No. 1, p. 3.

[34] U. Ma and D.T. Gawne, Wear of electroless nickel–phosphorus coatings, *Trans. IMF*, 63(1985), No. 1, p. 64.